# Monte Carlo study of electronic transport in $Al_{1-x}Ga_xAs/GaAs$ single-well heterostructures

Kiyoyuki Yokoyama and Karl Hess

*Coordinated Science Laboratory, University of Illinois at Urbana-Champaign, Urbana, Illinois 61801*

A study of electronic transport in $Al_{1-x}Ga_xAs/GaAs$ single-well structures including multisubband conduction at 77 and 300 K has been performed. The electronic states of the quantum well are calculated self-consistently taking the five lowest subbands into account. The numerically obtained wave functions and energy levels are used to obtain the major two-dimensional scattering rates in each subband. Polar optical- and acoustic-phonon (via deformation-potential) scattering are considered including intersubband transitions. For ionized impurity scattering, the screening effects due to the five lowest subbands are taken into account to obtain the Fourier-transformed Coulomb potential. The steady-state and transient behavior of the electrons in the well are studied through a Monte Carlo particle simulation. It is shown that high transient velocities $[(3-8) \times 10^7$ cm/sec] can be expected at low and intermediate fields.

## I. INTRODUCTION

Enhanced electron mobility in modulation-doped $Al_{1-x}Ga_xAs/GaAs$ heterostructures has been suggested by Esaki and Tsu[1] and demonstrated independently by Dingle, Störmer, Gossard, and Wiegmann.[2] Subsequently, much attention has been focused on modulation-doped heterostructures in order to realize ultra-high-speed field-effect devices, such as the high-electron-mobility transistor (HEMT).[3] Among some other combinations of III-V compound semiconductors, the largest effort has been devoted to study the $Al_{1-x}Ga_xAs/GaAs$ system.[4]

In this system, the $Al_{1-x}Ga_xAs$ layer is doped $n$ type, while the adjacent GaAs layer is grown as pure as possible (not intentionally doped). The free electrons are transferred to the high-purity GaAs layer where they populate a narrow potential well and form a quasi-two-dimensional electron gas (Q2D EG). Since the electrons are spatially separated from the ionized donors, they exhibit a high-electron mobility even at high carrier densities. In fact, very impressive high-mobility values have been reported.[5-7] It has also been demonstrated that single period heterostructures exhibit better low-field mobilities than multiple heterolayers.[8]

Not only experimental but also theoretical work has been stimulated to understand electronic transport in heterolayers. Investigations of quasi-two-dimensional systems[9] have originally been performed for the inversion layers of metal-oxide-semiconductor field-effect transistors (MOSFET's). Following the pioneering studies of Stern and Howard for MOSFET's,[10] Ando carried out detailed calculations of MOSFET's and $Al_{1-x}Ga_xAs/GaAs$ single-well structures.[11] In these studies, the subband structure has been calculated using wave functions and energy levels which are obtained by a self-consistent calculation based upon the effective-mass approximation.

Simultaneously, lattice scattering[12-16] and impurity scattering[14,16-19] for electrons in heterolayers have been extensively investigated. Many of the above treatments

have assumed square-well potentials and approximate wave functions to express the scattering rates analytically. Walukiewicz, Ruda, Lagowski, and Gatos[20] used a triangular-well approximation to discuss the electron mobility more realistically. For impurity scattering in Si inversion layers, Mori and Ando reported formulas using variational functions.[17] However, they focused their attention upon low temperatures to discuss the ultimate limits of the mobility values. Their final results are not applicable at high temperatures.

In all previous publications, the electron mobility values have been calculated from a relaxation time which is closely related to the inverse of the scattering rate. For device applications, we need to understand the warm- and/or hot-electron behavior of the quantum well system at and above 77 K. To study the transport properties in this regime, the Boltzmann transport equation must be solved taking into account the scattering in each subband of the $Al_{1-x}Ga_xAs/GaAs$ single-well potential. A Monte Carlo method[21] can bypass the difficulties in directly solving the complicated system of equations. Hot-electron velocity characteristics for a strictly two-dimensional system confined in a square well of $Al_{1-x}Ga_xAs/GaAs$ have already been studied previously using the Monte Carlo method.[22]

In this paper, we present more precise calculations of electron transport properties for $Al_{1-x}Ga_xAs/GaAs$ single-well heterostructures including multisubband conduction by means of an ensemble Monte Carlo method. In Sec. II, the electronic states of the quantum well are calculated self-consistently taking the five lowest subbands into account. The numerically obtained wave functions and energy levels are used to calculate the major two-dimensional scattering rates at 77 and 300 K in Sec. III. Polar optical-phonon scattering and acoustic-phonon scattering (via the deformation potential) are studied for each subband including intersubband transitions. For ionized impurity scattering, the screening effects due to the five lowest subbands are considered to calculate the

Fourier-transformed Coulomb potential. The squared matrix element, which is calculated from the Fourier-transformed Coulomb potential, accounts for both remote and background impurity scattering. The results of Sec. III are used to calculate the transport properties of the electrons by using the Monte Carlo method which is described in Sec. IV. Steady-state and transient characteristics of the electron drift velocities are discussed in detail together with average electron energy and population of each subband and the subsidiary minima ($L, X$).

## II. THE ELECTRONIC STATES
## OF SINGLE-QUANTUM-WELL STRUCTURES

In the triangular-well approximation, the quantized energy levels are proportional to the inverse cubic root of the effective mass. Since the effective masses in the subsidiary valleys are larger than in the $\Gamma$ valley, size quantization effects are small in the $L$ or $X$ valleys. Therefore, we account for size quantization effects only in the $\Gamma$ valley.

Self-consistent numerical calculations are performed to obtain the quantized energy levels and the corresponding wave functions for an actual single-well heterostructure following Ref. 23. These numerically obtained results are used to calculate the major two-dimensional scattering rates in each subband, as described in the next section.

The wave function parallel to the heterointerface ($xy$-plane) is assumed to be a plane wave. The envelope function normal to the layer interface ($z$ direction), $F_m(z)$ for the $m$th subband, satisfies the following Schrödinger equation:

$$-\frac{\hbar^2}{2m^*}\frac{d^2F_m(z)}{dz^2}+V(z)F_m(z)=E_mF_m(z) \ . \tag{1}$$

The effective potential $V(z)$ is given by

$$V(z)=-e\phi_e(z)+V_h(z)+V_{xc}(z) \ , \tag{2}$$

where $\phi_e(z)$ is the electrostatic potential given by the solution of Eq. (3) below, $V_h(z)$ is the step function describing the interface barrier, and $V_{xc}(z)$ is the local exchange correlation potential.[24] We take into account the five lowest subbands. Then, Poisson's equation reads

$$\frac{d^2\phi_e(z)}{dz^2}=\frac{e}{\epsilon_0\epsilon}\left[\sum_{i=1}^{5}N_iF_i^2(z)+N_A(z)-N_D(z)\right] \ , \tag{3}$$

where $N_i$ represents the number of electrons in subband $i$ and is given in equilibrium by

$$N_i=\frac{m^*k_BT}{\pi\hbar^2}\ln\left[1+\exp\left[\frac{E_F-E_i}{k_BT}\right]\right] \ . \tag{4}$$

$N_A(z)$ and $N_D(z)$ are the position-dependent acceptor and donor concentrations, and $E_F$ is the Fermi energy.

We use an effective mass $m^*=0.067m_0$ and a dielectric constant $\epsilon=12.9$ in both GaAs and $Al_{1-x}Ga_xAs$. This approximation may be inappropriate under certain circumstances which include a high Al content and a deep penetration of the wave function into the $Al_{1-x}Ga_xAs$. The uniform dielectric constant is equivalent to the neglect of the image force in Eq. (2). We have also as-

TABLE I. Assumed parameters of $Al_{1-x}Ga_xAs$/GaAs structure.

| Layer | Material | $N_D$ (cm$^{-3}$) | $N_A$ (cm$^{-3}$) | Thickness (nm) |
|---|---|---|---|---|
| I | GaAs | 0 | $1\times10^{15}$ | 1000 |
| II | $Al_{0.3}Ga_{0.7}As$ | 0 | $1\times10^{14}$ | 10 |
| III | $Al_{0.3}Ga_{0.7}As$ | $5\times10^{17}$ | $1\times10^{14}$ | 40 |

sumed abrupt interfaces, and a barrier height of 0.3 eV. All of these approximations are very reasonable according to the results reported by Stern and Das Sarma.[23] Moreover, the $Al_{1-x}Ga_xAs$ layer is assumed to be depleted of mobile charge except for the penetration of the wave function of electrons from the GaAs. Owing to the above-mentioned assumptions, the problem is greatly simplified and we can use the Numerov method[25] to solve the Schrödinger equation. This algorithm is efficient to obtain the pairs of eigenvalues and eigenfunctions accurately within short computational times.

The parameters of the computation are summarized in Table I. In the calculation the origin of the $z$ coordinate is chosen at the heterointerface between regions I and II and the inversion carrier density $N_s$ is taken to be $5\times10^{11}$ cm$^{-2}$. The Poisson's equation is solved for the three regions shown in Fig. 2. Since quantization is only important at the well region, Eq. (1) is solved from $z=-20$ to 100 nm to save computational time and memory space. An iterative scheme is used to solve the above described system of Eqs. (1)–(4). The initial conditions of the binding energies and the corresponding wave functions are calculated analytically under the triangular potential approximation, where the wave functions are expressed by Airy functions. The effective potential calculated from Eq. (2) is updated as[26]

$$V_{in}^{(n+1)}(z)=V_{in}^{(n)}+f^{(n+1)}W^{(n)}(z) \ , \tag{5a}$$

$$W^{(n)}(z)=V_{out}^{(n)}(z)-V_{in}^{(n)}(z) \ , \tag{5b}$$
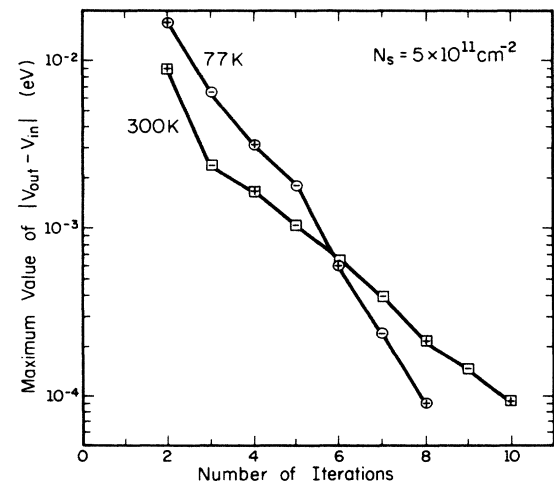


FIG. 1. Illustration of convergence process for calculating the self-consistent solutions assuming the deceleration factor $f=1$ in Eq. (5a). The signs in the figure indicate the sign of Eq. (5b).
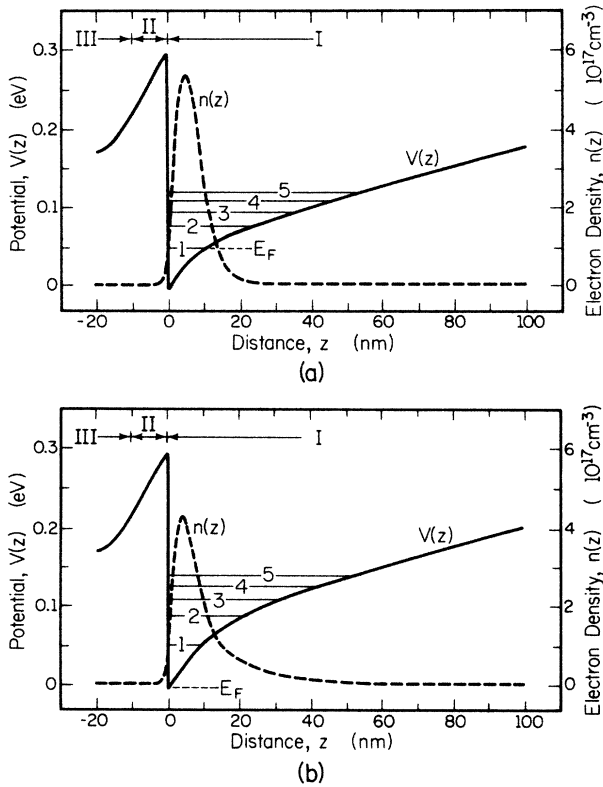
FIG. 2. Calculated effective potential defined by Eq. (2) and electron density distribution at (a) 77 K and (b) 300 K. The numbers in the figure indicate the quantized energy levels of the five lowest subbands.

TABLE II. Binding energies and electron population.

| mth subband | 77 K | | 300 K | |
|---|---|---|---|---|
| | $E_m$ (meV) | Population (%) | $E_m$ (meV) | Population (%) |
| 1 | 47.5 | 98.0 | 50.3 | 68.0 |
| 2 | 76.2 | 1.8 | 85.9 | 17.8 |
| 3 | 93.5 | 0.1 | 107.7 | 7.7 |
| 4 | 107.5 | | 124.1 | 4.1 |
| 5 | 119.8 | | 137.9 | 2.4 |
| $E_F$ | 64.1 | | 35.9 | |

where the subscript indicates the iteration number. The artifical deceleration factor $f$ is generally introduced to obtain the solution safely.

Figure 1 shows the convergence process for the self-consistent calculation at 77 and 300 K assuming $f = 1$. Although the sign of the maximum value of Eq. (5a) is changing every iteration step, convergence is excellent.
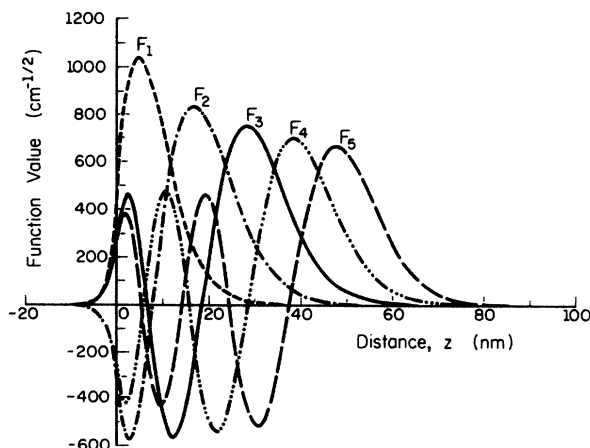
The convergence criterion used in our study is that the largest absolute value of Eq. (5a) must be less than $10^{-4}$ eV. By assuming a smaller value of $f$, it is possible to conserve the sign of Eq. (5a) during the iteration. The more sophisticated method is to guess a suitable $f$ in every iteration, which is efficient for ill-conditioned problems.[26] The use of $f \neq 1$ has been necessary for high carrier concentrations.

Figure 2 shows the effective potential calculated from Eq. (2) together with the five lowest subband energy levels at 77 and 300 K. The dashed line indicates the electron concentration which is derived from the first term in the large parentheses of Eq. (3). The corresponding wave functions for the first to the fifth subbands at 77 K are shown in Fig. 3. It can be seen from Figs. 2(a) and 2(b) that the electron density at 300 K is extending somewhat deeper into the substrate compared with the extension at 77 K. This means, of course, that the electrons at 300 K have higher probabilities to stay in the upper subbands than those at 77 K, as shown in Table II. Table II also shows the obtained energy eigenvalues for the five lowest subbands and the Fermi energy. The subband separations $E_2 - E_1$ for 77 and 300 K are 28.7 and 35.6 meV which are considerably greater than $k_B T$. It is evident from Table II that more than 85% of electrons are in the two lowest subbands in equilibrium. The results compare well with those reported by Vinter[27] at room temperature.

## III. MULTISUBBAND SCATTERING MODELS

The dominant scattering mechanisms for three-dimensional III-V compound semiconductors have been studied in detail.[28,29] Among various kinds of scattering mechanisms, phonon scattering and ionized impurity scattering play important roles to determine the transport properties. Lattice scattering and impurity scattering in heterolayers have also been extensively studied.[12-19] In this section, results for these quasi-two-dimensional scattering rates are derived using the self-consistent results for the potential well.

### A. Phonon scattering

The square of the matrix element for scattering between the mth and nth subbands is[15]

$$|M_{mn}|^2 = \int |M(Q,q)|^2 |I_{mn}(q)|^2 dq , \qquad (6)$$



FIG. 3. Calculated wave functions for the five lowest subbands at 77 K corresponding to Fig. 2(a).

where $M(Q,q)$ is the corresponding three-dimensional matrix element, and $Q = \pm(k_1 - k_2)$ and $q$ are the phonon wave-vector components parallel and perpendicular to the layer interfaces. $k_1$ and $k_2$ denote the initial- and final-state wave vectors and $Q = |Q|$. The overlap integral can be expressed as[15]

$$I_{mn}(q) = \int F_m(z)F_n(z)\exp(iqz)dz \,, \tag{7}$$

where $F_m(z)$ is the normalized envelope function which is given by the solution of Eq. (1) as shown in Fig. 3.

For polar optical-phonon scattering, $|M(Q,q)|^2$ is proportional to $1/(Q^2+q^2)$. Accordingly, the scattering rate is proportional to $H_{mn}(Q)/Q$, where the multisubband coupling coefficients are given by[16]

$$H_{mn}(Q) = \int \int dz_1 dz_2 F_{mn}(z_1)F_{mn}(z_2)$$
$$\times \exp(-Q|z_1-z_2|) \,. \tag{8}$$

Here $F_{mn}(z) = F_m(z)F_n(z)$.

We have studied previously the difference of the coupling coefficient between the analytical approximation and the precise numerical approach both for intrasubband and intersubband transitions.[30] We also have shown that the wave functions are not too sensitive to temperature and the inversion carrier density. Therefore, the tabulated values of $H_{mn}(Q)$ as given in Ref. 30 have been used in the present calculation.

Using the matrix elements, the scattering rate is obtained from the golden rule:

$$S_{mn}^{\text{pop}} = \frac{e^2\omega_0}{8\pi\epsilon_0}\left[\frac{1}{\epsilon_\infty} - \frac{1}{\epsilon_s}\right](N_q + \tfrac{1}{2} \pm \tfrac{1}{2})$$

$$\times \int \frac{H_{mn}(Q)}{Q}\delta(E(k_2)-E(k_1)\pm\hbar\omega_0)dk_2 \,, \tag{9}$$

with

$$N_q = \left[\exp\left[\frac{\hbar\omega_0}{k_B T}\right] - 1\right]^{-1} \,. \tag{10}$$

Here $\epsilon_\infty$ and $\epsilon_s$ are the optical and static dielectric constant, $N_q$ is the phonon occupation number, and $\hbar\omega_0$ is the polar optical-phonon energy. The values used for $\epsilon_\infty$ and $\epsilon_s$ are 10.92 and 12.90, respectively, and $\hbar\omega_0$ is taken to be 35.4 meV. The $\pm$ signs stand for phonon absorption and emission, respectively. $E(k_1)$ and $E(k_2)$ denote the initial- and final-state energy. In the calculation, the total energy is measured from the bottom of the first subband. The energy levels listed in Table II are used to calculate the intersubband transitions. The integration over all final two-dimensional states $k_2$ is performed in polar coordinates (using $Q$ and the angle $\theta$ between $Q$ and $k_1$). Finally, the numerical integration is carried out and during this procedure the $Q$ value, which satisfies the delta function in Eq. (9), is used to look up the $H_{mn}(Q)$. The results of the numerical integration are finally built into a lookup table. To calculate the angular distribution, the rejection technique of von Neumann is employed by using a random number and the value of $H_{mn}(Q)/Q$, which is also obtained from our tabulation.

Equation (6) describes the interaction of quasi-two-dimensional electrons with bulk-mode phonons. That is, both contributions due to a half-space slab mode and surface-mode optical phonons[31] are approximated by the bulk-mode phonon. This treatment greatly simplifies the actual problem. Plausible as it may be, it is necessary to confirm this assumption for the given quantum well structure by estimating the contributions of surface optical phonons. The matrix element is proportional to $Q^{-1/2} \int \exp(-Q|z|)F_m(z)F_n(z)dz$, and a method analogous to the method reported by Hess and Vogl[32] for the Si-SiO$_2$ system can be applied to GaAs-Al$_{1-x}$Ga$_x$As structures to calculate the scattering rate. The detailed procedure will be reported in a forthcoming paper. The results for our structure can be summarized as follows. The intrasubband scattering rate for the surface mode is of the same order of magnitude as that for a slab mode. The scattering rate for the intersubband transitions is generally smaller than that for the intrasubband transitions due to the small value of the overlap integral. Therefore, for our material parameters, surface modes do not play any special role to cause specific intersubband transitions and our approximation of scattering by bulk phonons is fairly well justified.[33]

Deformation-potential acoustic-phonon scattering is treated similar to the optical-phonon scattering. The problem is, however, simpler in this case, because the matrix element in Eq. (6) is independent of $Q$. The scattering rate is given by

$$S_{mn}^{\text{acp}} = \frac{m^* k_B T D^2}{\hbar^3 \rho S_l^2} \int F_m^2(z)F_n^2(z)dz \,. \tag{11}$$

The GaAs material parameters used in the calculation are deformation potential $D = 7.0$ eV, density $\rho = 5.36$ g/cm$^3$, and the longitudinal sound velocity $S_l = 5.24 \times 10^5$ cm/sec. Equation (11) is valid for $E \geq E_m - E_n$, where $E$ is measured from the bottom of the $m$th subband. Notice that the acoustic-phonon scattering rates are independent of energy in the allowed energy range. Compared with the polar optical-phonon scattering rates, the acoustic-phonon scattering rates are very small. Therefore, we only take into account intrasubband transitions. In this case, the numerical integral, i.e., $2 \int F_m^4(z)dz = 1/b_{mm}$, represents the inverse of the effective well width for the $m$th subband.[34] Then, the scattering rates are inversely proportional to the well width.[12,14,15] In the simulation of transport, a uniform angular distribution is generated using random numbers. Notice that we have neglected piezoelectric coupling and screening of the interaction with acoustic phonons. We have also chosen a conservative value for $D$. These points are at present subject to some debate.[34,35] At any rate, additional studies are needed for nonlinear (and Ohmic) transport at very low temperatures (much below 77 K) and our present model is probably not very good in this temperature range.

The calculated phonon scattering rates for 77 and 300 K corresponding to Table I are summarized in Figs. 4 and 5, respectively.[36] Figures 4(a) and 5(a) show the scattering rates for the lowest subband together with the three-dimensional scattering rates,[28] and Figs. 4(b) and 5(b) indi-

cate the rates for the second subband. It should be noticed that the polar optical-phonon interaction in the quantum well is smaller than that of the corresponding three-dimensional system in the high-energy region. This is in contrast to a strictly two-dimensional system [delta-function limit for $F_1(z)$ (Ref. 14)]. Ferry pointed out that the scattering rate is generally reduced with the increase of the effective well width.[13] Similar results are also ob-

tained by approximating the wave function by sine functions.[37] The experimental results support the fact that the electron-phonon interaction in two-dimensional systems is smaller than that in three-dimensional ones.[38] However, the reduction may also be caused by screening and the effects of the degeneracy (Pauli exclusion principle), since the electron density in quantum-well structures is usually higher than in bulk experiments. However, a more rigorous model including phonon-plasmon coupling has not yet been developed.

## B. Ionized impurity scattering

Screened ionized impurity scattering in a single quantum well is computed by using the approach which has
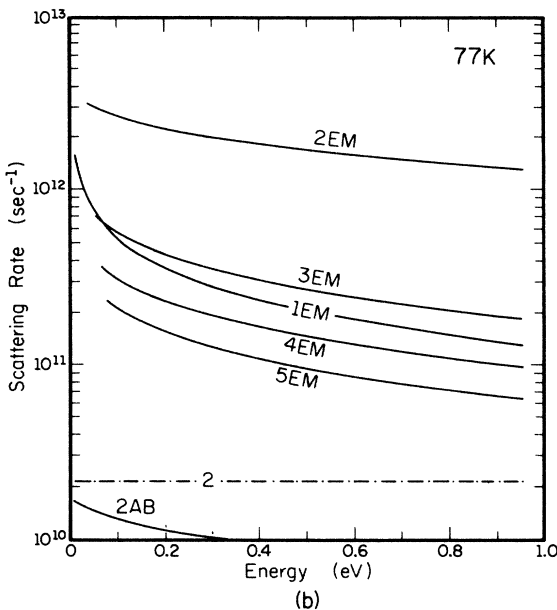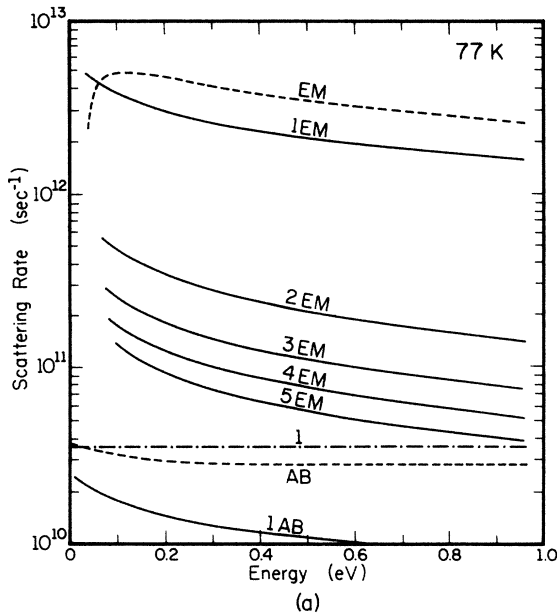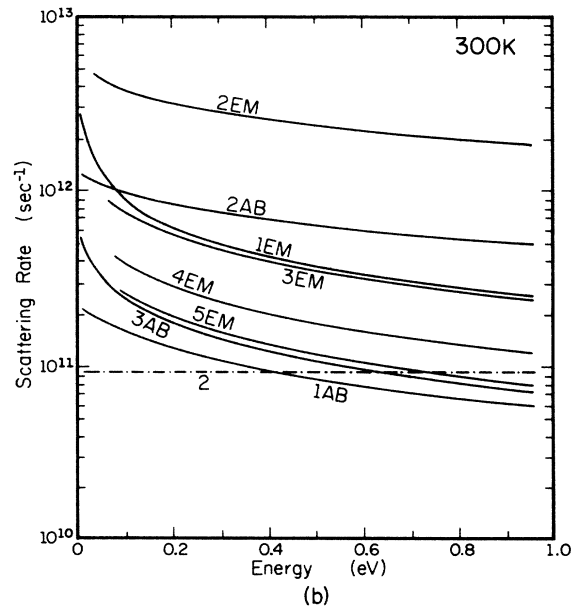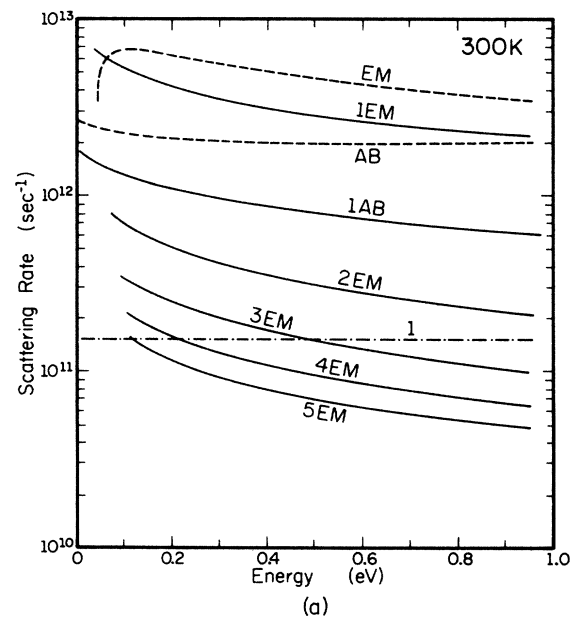


FIG. 4. Phonon scattering rates vs energy for (a) the first and (b) the second subband at 77 K. The numbers in the figure show the final subband. Solid lines show the rates for polar optical-phonon scattering, and EM and AB stand for emission and absorption, respectively. The dashed-dotted line indicates the rates for acoustic-phonon scattering. The scattering rates due to the three-dimensional polar optical-phonon interaction are also shown in Fig. 4(a) by the dashed lines. The energies are measured from the bottom of each subband.

FIG. 5. Same as Fig. 4 but for $T = 300$ K.

originally been proposed for MOSFET's by Stern and Howard.[10] The potential $\phi$ of a point charge located at $r=(0,z_0)$ is determined by the Poisson equation

$$\nabla^2\phi(r,z)-2\sum_i S_i g_i(z)\int \phi(r,z_1)g_i(z_1)dz_1$$

$$=-\frac{e}{\epsilon_0\epsilon_s}\delta(r)\delta(z-z_0) , \quad (12)$$

with

$$S_i=\frac{e^2}{2\epsilon_0\epsilon_s}\frac{N_i}{E_{di}} , \quad (13a)$$

and

$$E_{di}=k_B T\left[1+\exp\left[-\frac{E_F-E_i}{k_B T}\right]\right]$$

$$\times\ln\left[1+\exp\left[\frac{E_F-E_i}{k_B T}\right]\right] , \quad (13b)$$

where

$$g_i(z)=F_i^2(z) , \quad (13c)$$

$N_i$ is the two-dimensional carrier density expressed by Eq. (4), and $E_i$ is the energy level for the $i$th subband. Here $S_i$ is the screening constant, $E_{di}$ is called the diffusion energy, and $g_i(z)$ is the electron density function. The quantities represented by Eqs. (13) can be evaluated by using the results described in Sec. II. The second term of Eq. (12) shows the effects of screening on the impurity charge by the free carriers.

Multiplying Eq. (12) by $\exp(-i\mathbf{Qr})$ and integrating over $\mathbf{r}$, one can obtain

$$\left[\frac{\partial^2}{\partial z^2}-Q^2\right]\left[\phi(Q,z)-2\sum_{i=1}^{5} S_i g_i(z)\int dz_1\phi(Q,z_1)g_i(z_1)\right]$$

$$=-\frac{e}{\epsilon_0\epsilon_s}\delta(z-z_0) , \quad (14)$$

where the summation is taken over the five lowest subbands. Using the method of Green's functions, the Fourier-transformed Coulomb potential $\phi(Q,z)$ is written as[14]

$$\phi(Q,z)=-\int dz_1\frac{1}{Q}\exp(-Q\,|z-z_1|\,)$$

$$\times\sum_{i=1}^{5} S_i g_i(z_1)\int dz_2\phi(Q,z_2)g_i(z_2)$$

$$+\frac{e}{2\epsilon_0\epsilon_s Q}\exp(-Q\,|z-z_0|\,) . \quad (15)$$

Two approaches have been reported to solve Eq. (15) only for the lowest subband. One is that $g_i(z)$ is approximated by the delta function.[14] In the other approach, $g_i(z)$ is approximated by a sine function assuming a square-well potential.[19] In the present study, self-consistently calculated envelope wave functions are used to solve Eq. (15).

To estimate the initial value (for the numerical iterative procedure) of $\phi(Q,z)$, $g_i(z)$ is approximated by the delta function such that $g_i(z)\sim\delta(z-z_i)$, where $z_i$ shows the

position at which $g_i(z)$ assumes its maximum value,[39] and Eq. (15) is written as

$$\phi(Q,z)=-\frac{1}{Q}\sum_{i=1}^{5}\exp(-Q\,|z-z_i|\,)S_i$$

$$\times\frac{e}{2\epsilon_0\epsilon_s(Q+S_i)}\exp(-Q\,|z_i-z_0|\,)$$

$$+\frac{e}{2\epsilon_0\epsilon_s Q}\exp(-Q\,|z-z_0|\,) . \quad (16)$$

Here we have assumed that $\exp(-Q\,|z_m-z_n|\,)\sim 0$ for $m\neq n$. The approximation of Eq. (16) offers very good initial values especially for large $Q$. Using these initial values, Eq. (15) is solved iteratively.

The matrix element $M_{mn}(Q)$ for the electron-impurity interaction is obtained by

$$|M_{mn}(Q)|^2=\int M_{nn}^2(z_0)N_I(z_0)dz_0 , \quad (17)$$

with

$$M_{mn}(z_0)=\int e\phi(Q,z)F_m(z)F_n(z)dz , \quad (18)$$

where $N_I(z_0)$ represents the impurity concentration at $z=z_0$.
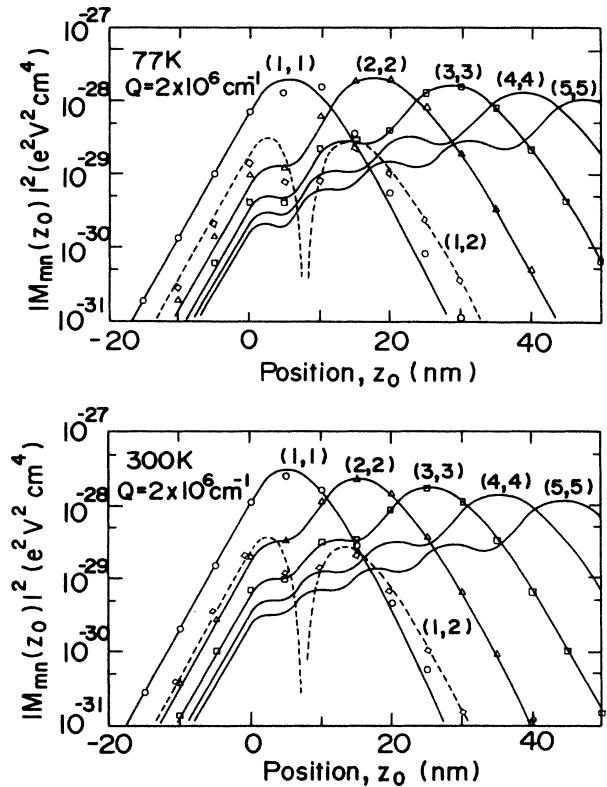
Figure 6 shows the calculated $|M_{mn}(z_0)|^2$ as a func-



FIG. 6. Calculated values of $|M_{mn}(z_0)|^2$ vs point-charge location $z_0$ for $Q=2\times10^6$ cm$^{-1}$ at (a) 77 K and (b) 300 K. The pair of numbers in the parentheses labels the initial and final subband. Symbols in the figure show the results obtained by using the analytical expression of Eq. (16) for the three lowest intrasubband transitions and the most important intersubband transition from the first to the second.

tion of the point-charge location $z_0$ for $Q = 2 \times 10^6$ cm$^{-1}$ at 77 and 300 K. The screening constants for the three lowest subbands in equilibrium (zero electrical field) are $1.81 \times 10^6$, $24.5 \times 10^4$, and $19.9 \times 10^3$ cm$^{-1}$ at 77 K, and $7.16 \times 10^5$, $2.36 \times 10^5$, and $1.03 \times 10^5$ cm$^{-1}$ at 300 K. The solid lines in Fig. 6 represent the scattering rate of intrasubband transitions, and the dashed line shows the values for the most dominant intersubband transitions between the first and the second subband. The peak locations for the intrasubband transition coincide with the $z_i$'s. The symbols illustrated in these figures correspond to the initial values which are derived from Eq. (16). It can be seen from Fig. 6 that Eq. (16) gives very good approximations for large $Q$ values. The agreement is especially good for subbands higher than the second. In equilibrium, the electron population in the first subband is dominant, as shown in Table II. Therefore, Eq. (18) must be solved especially carefully for the first subband. Moreover, the contribution of more than the lowest eigenstates must be considered for small $Q$ values. Since we have performed the integration of Eq. (18) numerically using the Fourier-transformed Coulomb potential, which is obtained as the exact solution of Eq. (15), the two important requirements described above are fulfilled in our calculation.

Using Eq. (18) and the impurity density $N_I(z_0)$ listed in Table I, the integration of Eq. (17) is also performed numerically. In this integration, the contributions due to remote impurity scattering $(z_0 < 0)$ and background impurity scattering $(z_0 < 0)$ are taken into account. Figure 7 shows the calculated values of $|M_{mm}(Q)|^2$ at 300 K. With the decrease of the $Q$ value, the values of $|M_{mm}(Q)|^2$ increase. However, the increase is weaker in regions of small $Q$.

Finally, the impurity scattering rate is obtained from

$$S_{mn}^{imp} = \frac{1}{2\pi\hbar} \int |M_{mn}(Q)|^2 \delta(E(\mathbf{k}_2) - E(\mathbf{k}_1)) d\mathbf{k}_2 . \quad (19)$$

The scattering rate and the angle distribution are calculated by looking up the prepared computer tables similar to the calculation described above for polar optical-phonon scattering.

The numerical results for scattering from the lowest subband to itself and other subbands are summarized in Fig. 8 for $T = 77$ and 300 K. In bulk material, ionized impurity scattering is one of the more important scattering mechanisms limiting the electron mobility. Due to modulation doping with a nonintentionally doped spacer layer, the scattering rates are very small, as shown in Fig. 8. Since most electrons are in the first subband, scattering in this subband is very important. It can be seen from Fig. 8(b) that the intersubband scattering rate is much smaller than the intrasubband scattering rate in the first subband. Notice that the absolute intersubband scattering rate due to ionized impurities is always small compared with other scattering mechanisms (especially phonon scattering). Therefore, we include below only intrasubband transitions due to ionized impurity scattering which gives

$$S_{mm}^{imp} = \frac{m^*}{\pi\hbar^3} \int_0^\pi M_{mm}(Q)^2 d\theta . \quad (20a)$$
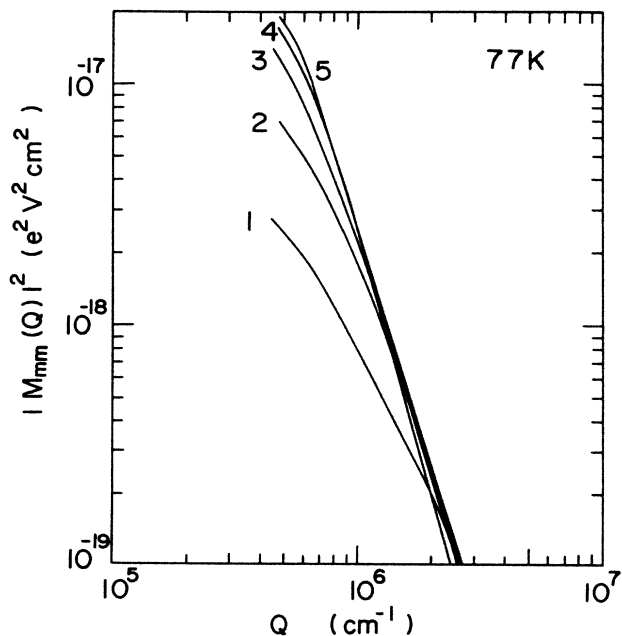


FIG. 7. Calculated square of matrix element $|M_{mm}(Q)|^2$ for intrasubband transition at 77 K. The numbers in the figure correspond to the subscript $m$.
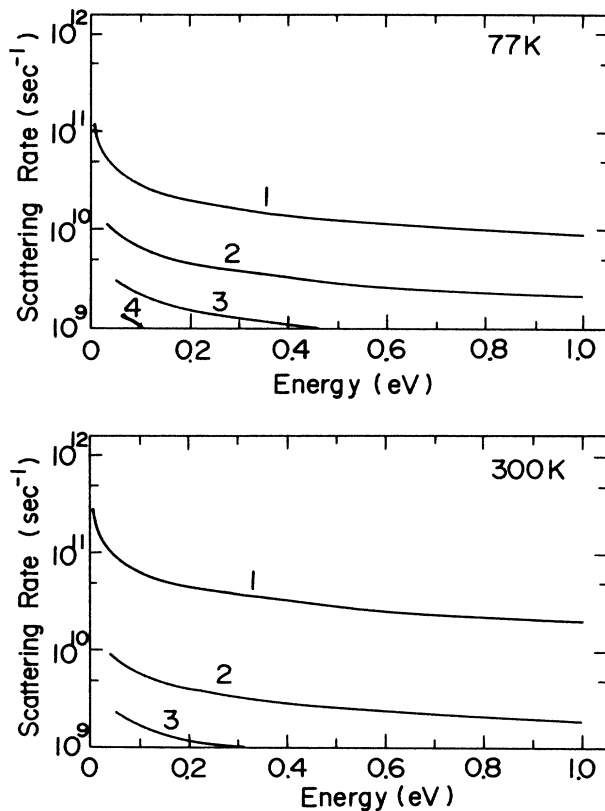


FIG. 8. Ionized impurity scattering rates for scattering in and out of the lowest subband (subband number 1) at (a) 77 K and (b) 300 K. The numbers in the figure show the final subband.

with

$$Q = 2k_1 \cos\theta ,$$     (20b)

where $k_1$ is the absolute value of $\mathbf{k}_1$, and $\theta$ is the angle between $\mathbf{Q}$ and $\mathbf{k}_1$.

## IV. TRANSPORT PROPERTIES

### A. Outline of Monte Carlo calculation

In our Monte Carlo study of electronic transport in single-quantum well structures, a uniform field is assumed along the heterointerface ($y$ direction), and the five lowest subbands around the $\Gamma$ point of GaAs are considered. Complete $\Gamma$-$L$-$X$ band structures are included for both GaAs and $Al_{1-x}Ga_xAs$ layers. Some of the material parameters have already been discussed in the previous two sections. Other necessary parameters are listed in Table 1 of Ref. 40, which are obtained either from experimental results or from pseudopotential calculations.

Two types of simulation are made to study steady-state and transient behavior. In the case of the steady-state analysis, the trajectory of one-particle motion is followed for a long period of time, and the steady-state transport properties such as average drift velocity and population of each subband and each valley are calculated from the history of electron motion. In this case, we do not need to specify initial conditions. The steady-state calculation is typically continued until the scattering events exceed 20 000 to obtain a good convergence in the estimation of average drift velocities and the like.

For the analysis of transient transport phenomena, many electrons must be simulated at the same time. The initial distribution of electrons plays an important role. We have generated the initial subband population and energy ($k$-vector values) in each subband based upon the results in Sec. II using the rejection technique of von Neumann. We have chosen 10 000 electrons for the simulation and a constant time step ($10^{-4}$ sec ) discretization scheme.[40] This scheme allows us to track the time evolution of the electron transport, and is also advantageous to updating the self-consistent calculation of electron states as the distribution function changes at a given instance of time.

The electrons in the $\Gamma$ valley of the GaAs layer are treated including the size quantization effects described in the above two sections, and those in the $L$ and $X$ valleys of the GaAs layer and those in the $Al_{1-x}Ga_xAs$ layer are treated as three dimensional. For an electron in each subband of the GaAs layer, 16 possible scattering mechanisms, which include ten polar optical-phonon scattering processes for emission and absorption (intersubband and intrasubband transitions), intrasubband acoustic-phonon transitions, intrasubband ionized impurity scattering, and intervalley scattering to the $L$ and the $X$ valleys, are tabulated. For a specific scattering event, one of the above described 16 mechanisms is chosen (proportional to each scattering probability at the given energy) by a generated random number.

As can be seen from Eqs. (3) and (4) as well as Eq. (13b), the distribution function influences both the form

of the well potential [Eq. (2)] and the screening constant [Eq. (13a)]. Therefore, it is necessary in principle to update well potential and screening as the energy distribution evolves in high electric fields. It is clear that a solution of Schrödinger equation for each Monte Carlo step (which is necessary in principle) requires enormous computational resources. We have therefore ignored the changes of potential well and screening in our calculation below. We are currently working on a simplified approach using an electron temperature (which is obtained from the average electron energy calculated by the Monte Carlo method) in Eqs. (4) and (13b). These more exact (but qualitatively very similar) results will be presented in a forthcoming publication.

The used models for nonequivalent intervalley scattering between the $L$ and the $X$ valleys, and equivalent intervalley scattering in the $L$ and the $X$ valleys are the same as those reported by Fawcett et al.[28] However, we have modified their approach for the transitions from the subbands in the $\Gamma$ valley to the subsidiary valleys (or vice versa). While we have used the same coupling constants (deformation potential scattering) as usually used in bulk GaAs, we have included the subband structure in the necessary summations over the density of final states (total scattering rate) and in the determination of the final states of a given scattering process. We have always properly accounted for the subband energy $E_m$ of the $m$th subband of the $\Gamma$ valley. The final-state subband is chosen (for the $L \to \Gamma$, $X \to \Gamma$ scattering process) randomly among all the subbands which are eligible by energy and momentum conservation rules.

These transitions between the size-quantized $\Gamma$ states and the $X$ and $L$ minima present a nontrivial problem even from a conceptual viewpoint because of the nonlocal character of the $L$ and $X$ states. Of course, size quantization also influences these states. However, the spacing of the energy levels (due to size quantization) is much smaller than at $\Gamma$ and the collision broadening (intervalley scattering) is much larger than at $\Gamma$ so that the three-dimensional approximation seems appropriate for these states. Electrons in the $X$ and $L$ valleys can then move away from the heterolayer interface against the self-consistent interface electric field. Our calculation ignores this effect as each $X$ and $L$ electron which is scattered back to $\Gamma$ ends up in any subband with equal probability as long as energy conservation permits.

An alternative procedure would be to view the $X$ and $L$ electrons as narrow wave packets. Our computation shows that the mean free path of these electrons is of the order of 50 Å. It seems therefore appropriate to trace the $X$ and $L$ electrons in real space and to permit only scattering to those subbands at $\Gamma$ whose wave function still shows significant overlap with the wave packet (overlap integral approximated by 1) and to put the transition probability equal to zero otherwise. As an example, we have performed a simulation assuming that the $\Gamma$-electron wave functions do not overlap with the $X$ and $L$ wave functions beyond the intersection of subband minima and potential well. The result of this way of calculation agrees for all cases discussed in this paper with the simplified method described above (within typically $\lesssim 10\%$). We

conclude, therefore, that our simplified model can be used with confidence.

All of the scattering mechanisms in the $Al_{0.3}Ga_{0.7}As$ are assumed to be three dimensional including polar optical-phonon and nonequivalent and equivalent intervalley scattering. In the calculation, the electrons are reflected or transmitted depending upon their kinetic and potential energy at the heterointerface.[40] As described in Sec. II, the structures and the operating conditions have been chosen in a way that there are virtually no mobile electrons in the $Al_{1-x}Ga_xAs$ layer. Therefore, the scattering mechanisms used in the $Al_{1-x}Ga_xAs$ layer are not too important in the present study.

## B. Numerical results

Calculated results for the steady-state behavior of the Q2D EG, which is confined in the potential well illustrated in Figs. 2(a) and 2(b), are shown in Figs. 9(a) and 9(b), for 77 and 300 K, respectively. These figures show that a large number of electrons populates the first subband at low electric fields. With the increase of the applied fields,
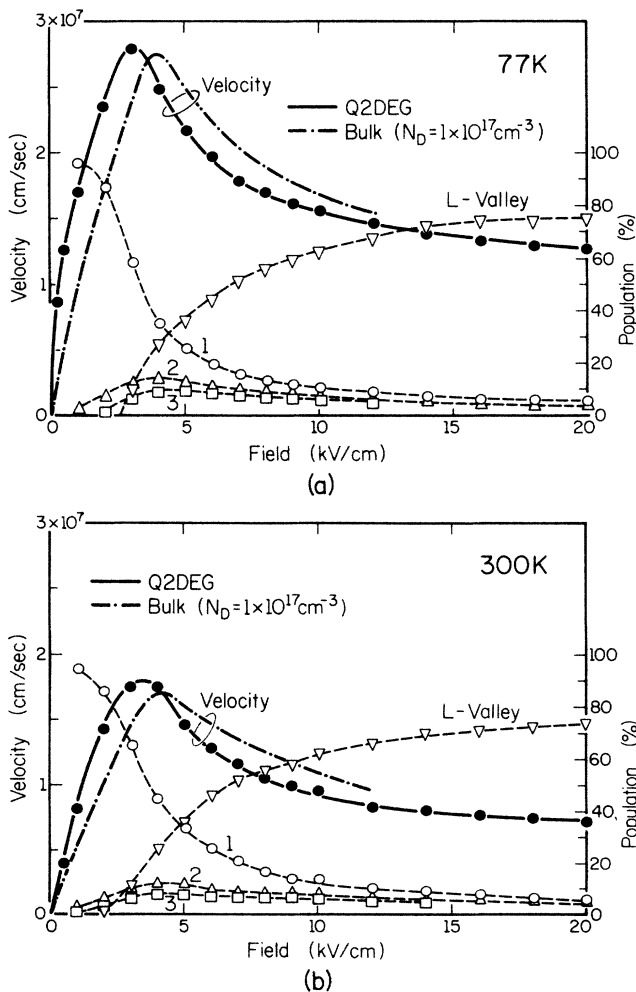


FIG. 9. Steady-state velocity and population vs field characteristics at (a) 77 K and (b) 300 K. The dashed-dotted curve represents the calculated velocity characteristics of Ref. 29 for three-dimensional transport.

the population of electrons in the first subband decreases and that in higher subbands increases. At still higher field, electron excitation to the subsidiary minima (at first $L$ valleys and then $X$ valleys) begins. The scattering rate in these upper valleys is larger than that in the $\Gamma$ valley, as is well known. In addition, the effective masses in the higher valleys are large. Therefore, the population in the $\Gamma$ valley, which is given by the sum over all subbands, and the drift velocity decrease with increasing electric field. Consequently, the steady-state characteristics for the Q2D EG are very similar to those for the three-dimensional gas.[29]

The peak carrier concentrations in the present calculation are $5.4 \times 10^{17}$ and $4.3 \times 10^{17}$ cm$^{-3}$ at 77 and 300 K, respectively, as shown in Fig. 2. Therefore, the velocity characteristics for the Q2D EG are compared in Fig. 9 with those for bulk GaAs with $N_D = 1.0 \times 10^{17}$ cm$^{-3}$ (Ref. 29) which are shown by the dashed-dotted line. Although the parameters of the calculation for the bulk[29] are different from ours (since we used a more precise band structure), the agreement of the velocity values is quite close at high electric fields. The critical field where the peak velocity is observed for the Q2D EG is shifted to lower fields compared with that for bulk GaAs. This shift is caused by the reduced impurity scattering for the Q2D EG. Furthermore, Fig. 9 clearly demonstrates that we can expect high velocity values for Q2D EG at low fields which is significant for device applications.

In our calculation, mobilities at 500 V/cm are $2.5 \times 10^4$ and $8.1 \times 10^3$ cm$^2$/V sec at 77 and 300 K, respectively. The value at 77 K is smaller than some of the measured values,[5-8] which deserves discussion. One of the reasons is the difference in the structures and induced carrier density. Furthermore, the low-field mobility at low temperature depends very strongly on the applied field, which is illustrated by the very steep nonlinear increase of the curve in Fig. z/a). According to the experimental report,[8] we can expect 4—5 times larger mobility values as the field approaches zero. Finally, as mentioned in Sec. III A, our small mobility values at 77 K may also be caused by our neglect of screening effects for polar optical-phonon scattering and the effects of the degeneracy. However, further investigations, including coupled plasmon-phonon scattering and the possibility of a perturbed phonon distribution, are necessary to obtain a clear understanding of this low-field—low-temperature region.

The transient drift velocity response at 77 and 300 K is shown in Figs. 10(a) and 10(b), respectively. The velocity for the Q2D EG exhibits the peak value after a time period which is nearly equal to that of bulk GaAs ($N_D = 1.0 \times 10^{18}$ cm$^{-3}$) (Ref. 22) at an electric field of 10 kV/cm and for 77 K. The peak value for the Q2D EG is higher than for the bulk. Notice also that there is a steeper velocity response compared with the equivalent bulk material, which is due to the reduction in ionized impurity scattering. With increasing electric field, the transient behavior for the Q2D EG also comes very close to that for the three-dimensional gas. This is confirmed by a transient population study for each subband and valley. Therefore, it is concluded that the velocity advantages for the Q2D EG are significant compared with bulk material

only at low and intermediate fields.

Interesting overshoot phenomena are observed even in the low-field case at 77 K, as shown in Fig. 10(a). The overshoot for a field of 1 kV/cm and the shoulders observed at early times at 3 and 5 kV/cm arise from the step in the scattering rate at the threshold of spontaneous phonon emission.[41] In this near-ballistic regime, electrons are heated up by the applied field, and are scattered by emitting optical phonons after they reach the optical-phonon energy $\hbar\omega_0$. Then they lose momentum and energy, and approach the steady state. The time to reach the velocity maximum, which corresponds to the required time to heat up the electron gas, decreases with increase in the field.

The velocity response at 300 K in low fields is different from that at 77 K. The reason is that the electrons at 300 K have sufficient thermal energy to populate higher subbands, and to emit phonons without much energy gain from the field. This is clearly demonstrated for the results at 1 kV/cm in Fig. 10(b).

At longer times, the heated electrons begin to be excited to higher subbands, as shown in Fig. 11(a) for 77 K. At the beginning of this stage, the population of electrons in the first subband decreases and that in higher subbands increases gradually. Initially, the velocity is still increasing, as shown in Fig. 11(a) for 3 and 5 kV/cm, because most of the electrons are still in the $\Gamma$ valley. At 300 K the population dynamics is somewhat different. The number of electrons in the first subband increases and that in higher subbands decreases at the beginning of the time response, as shown in Fig. 11(b). To understand this
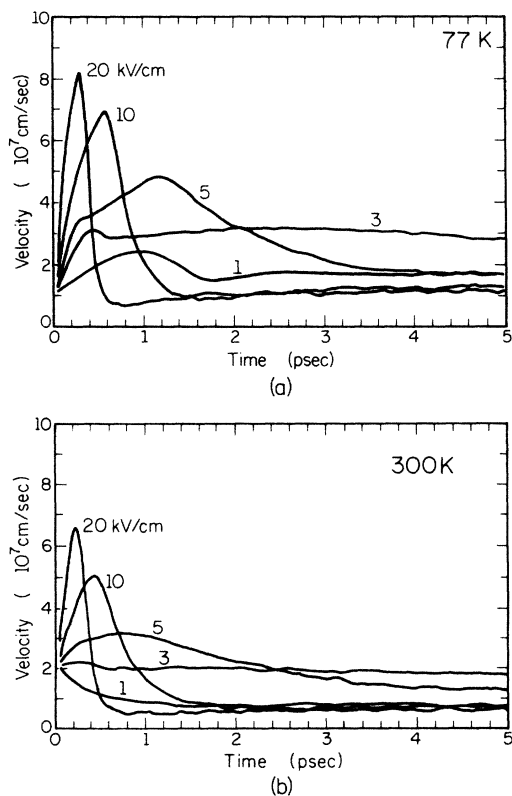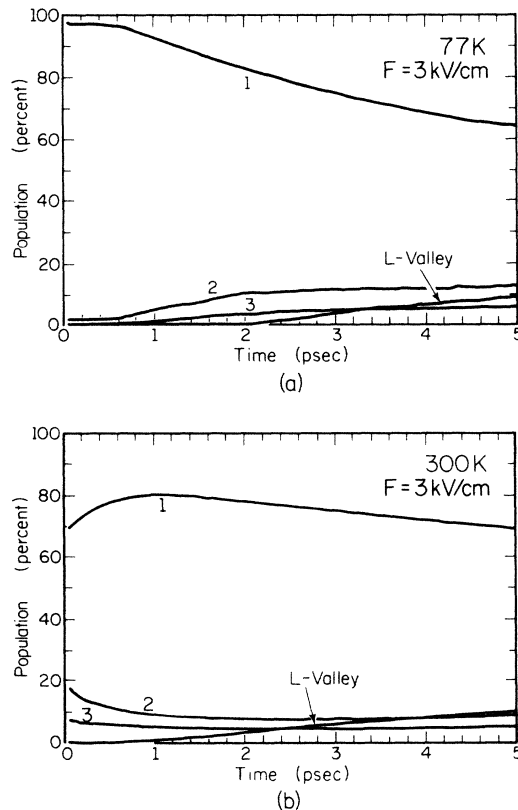


FIG. 11. Electron population in the three lowest subbands of the $\Gamma$ valley and the population of $L$ valleys for 3 kV/cm at (a) 77 K and (b) 300 K. The numbers in the figure label the subband.



FIG. 10. Transient velocity characteristics at (a) 77 K and (b) 300 K for different applied electric fields.

effect remember the second subband polar optical-phonon scattering rate as illustrated in Figs. 4(b) and 5(b). In the low energy region, the intersubband scattering rate from the second to the first subband is large. At 300 K, about 18% of electrons are in the second subband at zero field, as shown in Table II. The number at 77 K is much smaller than that at 300 K. Therefore, some electrons in the second subband are scattered to the first subband by emitting polar-optical phonons at 300 K after the field is applied.

As time progresses, electron excitation to the subsidiary minima begins to be important, as shown in Fig. 11. Then, the velocity decreases further. This causes the second velocity response peak for 3 kV/cm at 77 K and the main peaks for 5 kV/cm and above at both temperatures [Figs. 10(a) and 10(b)]. At $t = 5$ psec and 3 kV/cm, the population for the three lowest subbands for the $\Gamma$ valley and for $L$ valleys are 70.1%, 11.3%, 4.9%, and 7.3% at 77 K, and 74.3%, 8.2%, 5.1%, and 6.7% at 300 K, respectively.

We have also calculated the average electron energy in each subband and valley during the time transient. Figure 12 shows the average electron energy in the first subband at 77 K. Notice the curve for 1 kV/cm. This curve corresponds to the velocity response in Fig. 10(a). It can be seen that the above-described velocity overshoot in the initial near-ballistic region conforms to the energy response
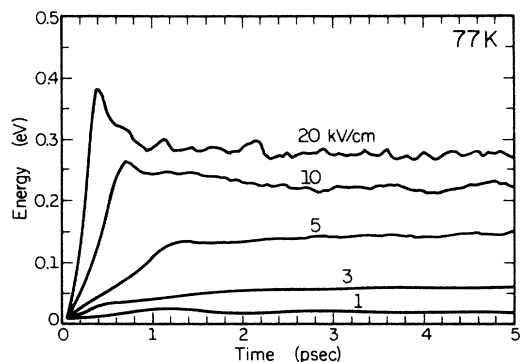
FIG. 12. Energy response in the first subband at 77 K.

shown in Fig. 12. Figure 12 also shows that the electrons in the first subband move to high energies almost instantaneously with the increase of the field. Subsequently, they are excited to the upper subbands and to the upper valleys, as shown in Fig. 9(a). The enhanced fluctuation of the average energy response in Fig. 12 at high fields is due to the reduction of the population in the first subband, because the average value becomes erroneous with decreasing the sampling numbers.

## V. CONCLUSION

Steady-state and transient calculations of electron transport properties of $Al_{1-x}Ga_xAs/GaAs$ modulation-doped heterostructures including the five lowest subbands have been reported at 77 and 300 K. Numerically obtained wave functions and energies for each subband have been used to calculate the major two-dimensional scattering rates, such as polar optical-phonon, acoustic-phonon via deformation potential, and ionized impurity scattering. Both intersubband and intrasubband transitions have been studied. In contrast to a strictly two-dimensional system, the obtained polar optical-phonon interaction in the quantum well is smaller than that for the corresponding three-dimensional system in the high-energy region. The calculated ionized impurity scattering rates, taking into account screening effects, are very small due to the modulation doping.

The steady-state and transient behavior of the electrons in the well has been investigated by a newly developed particle Monte Carlo simulator, which includes multisubband conduction. It has been confirmed that for the Q2D EG a drift-velocity response higher than in the bulk can be expected in the low-field region. In the high-field region, the velocity characteristics for the two-dimensional electron gas are very similar to those for the three-dimensional gas. However, the velocity responds more instantaneously after applying the field. Novel overshoot effects have been shown to occur, which are related to the population of the subbands and the subsidiary valleys. These velocity characteristics for the two-dimensional electron gas are advantageous for the realization of ultra-high-speed devices.

## ACKNOWLEDGMENTS

[1]L. Esaki and R. Tsu, IBM Research Center, Internal Research Report No. RC2418, 1969 (unpublished).

[2]R. Dingle, H. L. Störmer, A. C. Gossard, and W. Wiegmann, Appl. Phys. Lett. 33, 665 (1978).

[3]T. Mimura, S. Hiyamizu, T. Fujii, and K. Nanbu, Jpn. J. Appl. Phys. 19, L225 (1980).

[4]For review, see H. L. Störmer, Surf. Sci. 132, 519 (1983).

[5]S. Hiyamizu, J. Saito, K. Nanbu, and T. Ishikawa, Jpn. J. Appl. Phys. 21, L609 (1983).

[6]J. C. M. Hwang, A. Kastalsky, H. L. Störmer, and V. G. Keramidas, Appl. Phys. Lett. 44, 802 (1984).

[7]M. Heiblum, E. E. Mendez, and F. Stern, Appl. Phys. Lett. 44, 1064 (1984).

[8]M. Keever, W. Kopp, T. J. Drummond, H. Morkoc, and K. Hess, Jpn. J. Appl. Phys. 21, 1489 (1982).

[9]For review, see T. Ando, A. B. Fowler, and F. Stern, Rev. Mod. Phys. 54, 437 (1982).

[10]F. Stern and W. E. Howard, Phys. Rev. 163, 816 (1967).

[11]T. Ando, J. Phys. Soc. Jpn. 51, 3893 (1982).

[12]S. Kawaji, J. Phys. Soc. Jpn. 27, 906 (1969).

[13]D. K. Ferry, Surf. Sci. 75, 86 (1978).

[14]K. Hess, Appl. Phys. Lett. 35, 485 (1979).

[15]P. J. Price, Ann. Phys. (N.Y.) 133, 217 (1981).

[16]P. J. Price, Surf. Sci. 113, 199 (1982). See also B. K. Ridley, J.

Phys. C 15, 5899 (1982).

[17]S. Mori and T. Ando, Phys. Rev. B 19, 6433 (1979).

[18]E. Yamaguchi, J. Appl. Phys. 56, 1722 (1984).

[19]J. Lee, H. N. Spector, and V. K. Arora, J. Appl. Phys. 54, 6995 (1983).

[20]W. Walukiewicz, H. E. Ruda, J. Lagowski, and H. C. Gatos, Phys. Rev. B 30, 4571 (1984).

[21]For review, see C. Jacoboni and L. Reggiani, Rev. Mod. Phys. 55, 645 (1983).

[22]M. Tomizawa, K. Yokoyama, and A. Yoshii, IEEE Electron Device Lett. EDL-5, 464 (1984).

[23]F. Stern and S. Das Sarma, Phys. Rev. B 30, 840 (1984).

[24]L. Hedin and B. I. Lundqvist, J. Phys. C 4, 2064 (1971).

[25]P. C. Chow, Am. J. Phys. 40, 730 (1972).

[26]F. Stern, J. Comput. Phys. 6, 56 (1970).

[27]B. Vinter, Appl. Phys. Lett. 44, 307 (1984).

[28]W. Fawcett, A. D. Boardman, and S. Swain, J. Phys. Chem. Solids 31, 1963 (1970).

[29]J. G. Ruch and W. Fawcett, J. Appl. Phys. 41, 3843 (1970).

[30]K. Yokoyama and K. Hess, Phys. Rev. B 31, 6872 (1985).

[31]S. Q. Wang and G. D. Mahan, Phys. Rev. B 6, 4517 (1972).

[32]K. Hess and P. Vogl, Solid State Commun. 30, 807 (1979).

[33]This is not generally the case as pointed out by A. Pinczuk (private communication).

[34]P. J. Price, Phys. Rev. B **32**, 2643 (1985).

[35]W. Walnkiewicz, H. E. Ruda, J. Lagowski, and H. C. Gatos, Phys. Rev. B **32**, 2645 (1985).

[36]The effective well widths from the first to the fifth subband are 6.6, 11.0, 14.4, 17.3, and 19.8 nm for 77 K, and 6.1, 9.8, 13.1, 15.9, and 18.4 nm for 300 K.

[37]J. P. Leburton, J. Appl. Phys. **56**, 2850 (1984).

[38]J. Shah, A. Pinczuk, H. L. Störmer, A. C. Gossard, and W. Wiegmann, Appl. Phys. Lett. **42**, 55 (1983).

[39]The peak locations for the density functions from the first to the fifth subband are 4.8, 16.8, 28.2, 38.4, and 47.6 nm at 77 K, and 4.4, 14.8, 25.0, 35.0, and 44.2 nm at 300 K.

[40]T. Wang and K. Hess, J. Appl. Phys. **57**, 5336 (1985).

[41]K. Hess, IEEE Trans. Electron Devices **ED-28**, 937 (1981).